Implementation and Calibration of a Low-Cost Sensor Node for High-Resolution, Continuous and No-Manning Recording of Fruit Growth

Implementation and Calibration of a Low-Cost Sensor Node for High-Resolution, Continuous and No-Manning Recording of Fruit Growth

Lorenzo Mistral Peppi, Matteo Zauli, Luigi Manfrini*, Luca Corelli Grappadelli*, Luca De Marchi, Pier Andrea Traverso
DEI - Department of Electrical, Electronic and Information Engineering "Guglielmo Marconi"
**DISTAL - Department of Agricultural and Food Science and Technology*
40136 Bologna, Italy. Corresponding author: lorenzomistral.pepp2@unibo.it

***Abstract*—This paper describes a low-cost sensor node prototype for in-field, non-invasive fruit growth measurement, with particular emphasis on the calibration procedures required to obtain a significant improvement in stability when environmental conditions change and, thus, optimized performance. Despite the low-cost components used, the prototype allows to continuously monitor the variations in fruit size during night/day and irrigation/chemical cycles with an effective resolution lower than one millimeter. The full-scale implemented achieves 12 cm, overcoming the need of relocating the sensor during the ripening season, as instead typical of high resolution alternative solutions.**

I. Introduction

Real-time measurement of fruit diameter during all the phases of the growth season provides useful information, which can be used not only by farmers to estimate crop health and to implement actions for optimizing the use of irrigation and chemicals, but also for research purposes, e.g., to evaluate the tree water status as well as in models developed to manage orchard irrigation [1] [2].

However, farmers are often reluctant to uptake of electronic devices in farming due to the complexity and high costs that usually characterize these products, in addition to a not always understood added value conveyed by the adoption of sensor network for agricultural purposes.

Different systems (in several cases commercially available) to continuously measure the fruit growth have been developed making use of Linear Variable Displacement Transducer (LVDT) [3], strain gauges [4] and linear potentiometers [5]. These sensors are characterised by a very high resolution despite a very small measurable length. So relocation (requiring human works) every few days is needed. Other systems are developed using optical readers [6]. These do not require relocation, but the resolution is usually very low compared to previous ones, so that day and night fruit growth um-range variations cannot be perceived.

In this paper a simple low-cost but high-accuracy measurement device is presented, which is capable of recording, continuously and in a non-invasive nor destructive way, the growth of a fruit without the need for any relocation during the whole growth process. In addition, the performance of the system is strongly immune to environmental conditions. Due to these characteristics, a set of these sensors can be easily deployed throughout the orchard with a fine sampling step along its area.

The operating principle of the system and its architecture will be detailed, by focusing the discussion directly on the prototype that has been fully implemented. The calibration procedure exploited for the compensation of all main sources of uncertainty will be discussed, in addition to the analysis showing where these sources can be identified within the prototype. Experimental results will be presented for the validation of the architecture.

This work was funded by the "Italian Departments of Excellence" Initiative sponsored by the Italian Ministry of University (MUR).

II. System Architecture and Prototype

A. Operating principle of the system

The fruit to be measured is placed between two arms of the plier (Fig. 2), by means of retains jointed at the arm ends. The arms are linked together with a small bolt and retained with a spring. A potentiometer, which is supplied by a reference voltage also supplied to a micro-controller unit (MCU) and whose response V_{out} is A/D acquired by the same MCU, is stuck into a retain fixed to an arm, and a shaft connect the potentiometer to the other arm. In this way, it is possible to convert the aperture angle α into the linear distance d that represents the measurand according to:

$$d = 2 \cdot R \cdot \cos\left(\frac{\pi}{2} - \frac{\alpha(V_{out})}{2}\right) \tag{1}$$

in which R is the length of plier arm. The value of α is linearly dependent on the partition ratio, thus on the potentiometer output voltage. The MCU can perform all the calibration steps described in the following section, and store long records of data about fruit diameter evolution to be transmitted (e.g., on a daily rate) at a central node for further analysis.

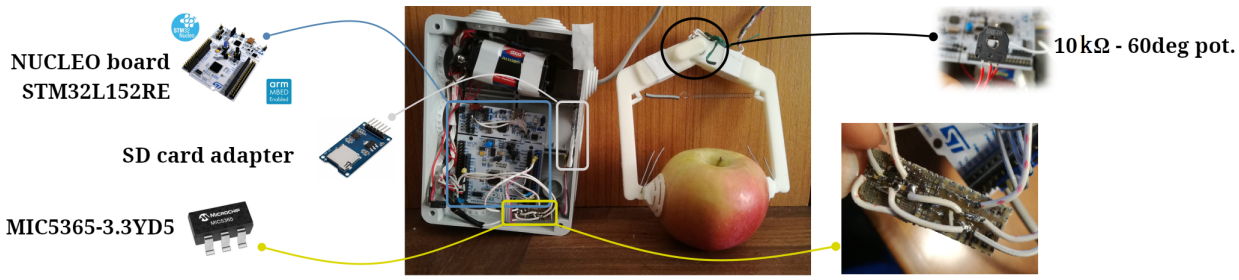

Fig. 1. The prototype implemented for no-manning high-resolution monitoring of fruit growth.

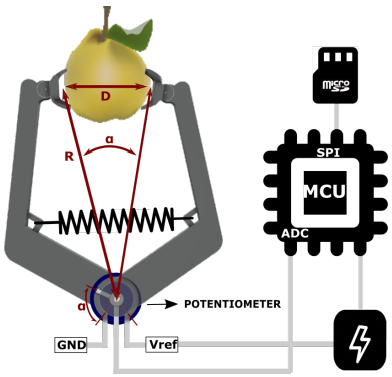

Fig. 2. Architecture of the proposed sensor node.

B. Prototype

A TRL-7 prototype of the sensor node concept in Fig. 2 has been fully implemented (Fig. 1).

The system is composed of different units: a potentiometer-based angular sensor, a plier to catch the fruit to measure, a MCU for data acquisition and processing, a micro-SD card adapter and a linear DC/DC converters used to generate the 3.3-V reference, required both for the system and to supply the angular sensor.

- As angular sensor a single-turn resistive potentiometer is used, connected as a simple voltage divider. Because of the potentiometer location on the pivot of the plier, variations of the aperture angle modify the partition ratio. In this way the distance between the two arms of the plier - the measurand - is transduced into a voltage V_{out}. The angle range of the potentiometer must be matched to the maximum aperture of the plier, in order to use the whole full-scale offered by the ADC stage in the MCU. The commercial component found to be the optimal choice was the PHS11-1DBR10KE60, manufactured by TT Electronics.
- The plier was manufactured making use of a 3D printer. The material used is Acrylonitrile Butadiene Styrene (ABS) to ensure light-weight: warping of the fruit, caused by the weight of the measurement system, must be strongly avoided, in order to minimize the perturbation due to the sensing on the fruit diameter time-evolution during night/day and irrigation/chemical cycles. Moreover, ABS ensures environmental stress resistance, as well as ease of printing and low cost. The arm length is $12\,\mathrm{cm}$, allowing for the monitoring of fruits like apples.
- As micro-controller, a STM32L152RE was selected because of the low-power capabilities of its core and the availability of a 12-bit, successive-approximation ADC on the same package. The micro-controller is implemented on a NUCLEO board, but the system can be further miniaturized by means of custom board design. In order to take advantage of the whole dynamic range of the ADC, and to compensate for dispersion effects on the voltage reference, the full-scale voltage provided to the latter ($3.3\,\mathrm{V}$) is the same used to bias the potentiometer (see Fig. 2). The nominal resolution of the sensor, approximately $30\,\mu\mathrm{m}$, is defined by the ADC nominal quantization step, whose value is $806\,\mu\mathrm{V}$. A temperature sensor is available within the MCU, which can be interrogated by the same ADC and is used for the real-time thermal dispersion compensation described in sec. III. A calibration set of coefficients for this sensor is extracted during the manufacturing process of the MCU, and these values are made available in a read-only register in order to get a more accurate temperature measurement. Nevertheless, this sensor has been compared (see Fig. 3), as a reference, to the HTS221 made by STMicroelectronics, a commercial temperature sensor characterized by a temperature accuracy of $\pm 1\,^{\circ}\mathrm{C}$ in the range $0/60\,^{\circ}\mathrm{C}$. The maximum estimated peak-to-peak deviation between the two sensors is $2.62\,^{\circ}\mathrm{C}$ over the range $24/72\,^{\circ}\mathrm{C}$. Such a small variation is not significant in order to perform a thermal compensation. Thus, the calibration process is made using the internal temperature sensor which is considered to be suitable for this purpose.
- A stable, low-noise power supply is required. At the same time, power saving strategies must be implemented. For these reasons, linear Low-Drop-Out (LDO) DC/DC converters are used. The first one, a LD39050PU33R from STMicroelectronics, available in the NUCLEO board, is exploited for powering the MCU. This device guarantees very high performance in terms of thermal stability and output noise ($30\,\mu\mathrm{V_{RMS}}$ over $10\,\mathrm{Hz}$ to $100\,\mathrm{kHz}$ bandwidth). Potentiometer and SD card adapter require to be powered only when used. For this reason, two additional LDOs, namely, MIC5365-3.3YD5-TR from Microchip with enable input, are used. It is worth noting that this

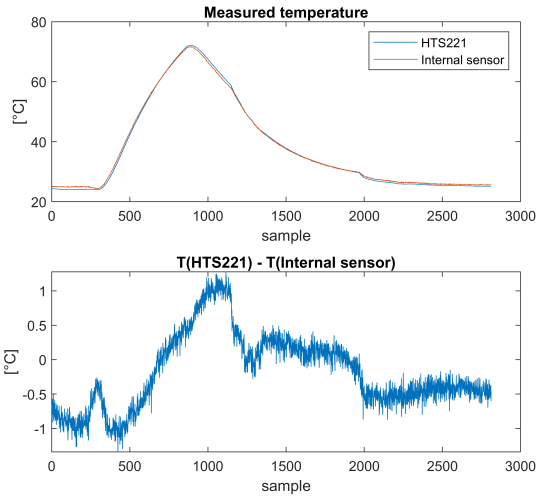

Fig. 3. Comparison between the MCU internal temperature sensor and the reference HTS221. Below: deviations with respect to the reference.

LDO shows worse thermal stability with respect to the STM one. This aspect will be discussed later.

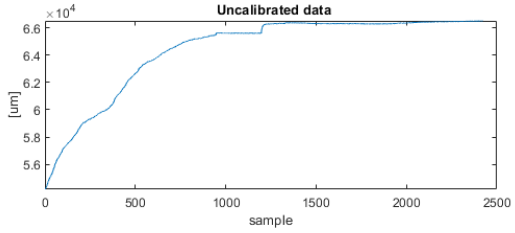

Fig. 4. Typical uncalibrated data acquired by the sensor during a 1-cm variation of the measurand on a 7-hour time scale.

A typical example of uncalibrated data acquisition can be seen in Fig. 4.

III. Calibration Procedure

Different sources of uncertainty can be identified in the uncalibrated sensor. However, since the latter has to operate in the most different environmental conditions, outdoor and under direct sunlight, during spring and summer, when the vast majority of fruits is growing, with daily thermal excursion that can easily reach dozens of °C, thermal stability is a must for this type of systems and dispersion due to temperature variations will be mostly addressed in the following.

A. A/D acquisition and averaging

Before addressing the thermal dispersion analysis, details regarding the A/D acquisition process and the compensation of short-term instabilities are provided. At each interrogation on the fruit diameter, the ADC is activated and M sequences of N samples of V_{out} are acquired in continuous mode, each sample converted by Eq. (1) into the uncalibrated reading $d_{R,n}^{(m)}$, in which (n, m) indicate the *n-th* sample of the *m-th* sequence. The estimator $\overline{d}_{\text{R}}$ of Eq. (2) is then computed, with an averaging of all the acquired samples in order to reduce short-time fluctuations and additive noise.

$$\overline{d}_{\text{R}} = \frac{1}{N * M} \sum_{m=1}^{M} \sum_{n=1}^{N} d_{R,n}^{(m)} \tag{2}$$

A trade-off between accuracy and power consumption must be considered when choosing the values of N, M and the ADC sampling period. Different multiples of the converter clock can be selected choosing predetermined values starting from $4 * ADC_{\text{clock period}}$ up to $384 * ADC_{\text{clock period}}$. The higher value causes the conversion time to be too long and results in an higher power consumption; this value is therefore excluded. Other values have been tested by analyzing, for each setting, the standard deviation of the estimator $\overline{d}_{\text{R}}$. For comparison purposes the results for four different tested values are depicted in Fig. 5. The value of N, representing the lowest number of samples that can be read during a single acquisition, is fixed to 250. For a given value of M the longer the sampling time, the lower the computed standard deviation, and the same effect can be achieved increasing the value of M.

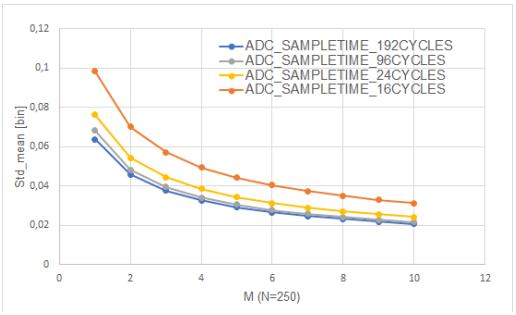

Fig. 5. Standard deviation of the estimator in Eq. (2) for different values of M and ADC sampling period. Vertical axis expressed in ADC bins (1 bin = 30 μm).

The actual number of samples is selected by varying the value of M, and the best trade-off with power consumption was found with M = 10 and sample period equal to 96 clock cycles. In this way, the standard deviation of the estimator in (2) is found to be negligible with respect to the other sources of uncertainty, while the power consumption to obtain each estimate $\overline{d}_{\text{R}}$ is still very low.

B. Sources of thermal dispersion

The strategy employed to determine to which extent every component is involved into the overall dispersion of the output data due to temperature is simple: exposing only some parts of the system in a place where the temperature is changing under control and recording the output, while all the other blocks are kept in constant environment conditions, will show how the firsts are influenced.

During the first test, only the potentiometer undergoes a forced heating and cooling cycle. The resulting data in Fig. 6, which are averaged according to the strategy described in sub-section III-*A* suggest, as expected, that the partition ratio is not affected by temperature, except for some very

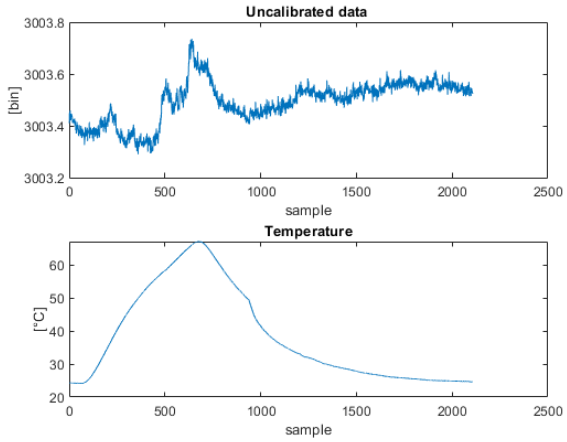

Fig. 6. Test with only the potentiometer under heating and cooling cycle. Above: averaged readings (Eq. (2)) expressed in ADC bins (1 bin = 30 μm). Below: corresponding temperature cycle.

small variations probably caused by inertia. This source of uncertainty is overally negligible.

During a second test, the potentiometer is kept at room temperature and fed directly by the power rail used to supply the ADC stage, while the NUCLEO board is heated. In this way, both the power supply stage and the ADC are affected by temperature variations, but only ADC dispersion is evaluated since its reference voltage is the same used for potentiometer. Results of this test are depicted in Fig. 7.

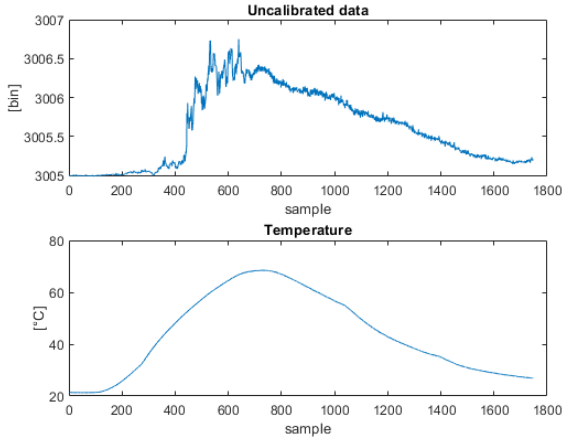

Fig. 7. Test with only the board under heating and cooling cycle, and with a supply strategy that allows to point out the ADC dispersion in temperature only. Above: averaged readings (Eq. (2)) expressed in ADC bins (1 bin = 30 μm). Below: corresponding temperature cycle.

Finally, the overall system was placed into the climatic chamber, by strictly fixing the plier aperture to a constant value near to the full scale, in order to test the prototype behaviour vs temperature. Averaged data acquired are depicted in Fig. 8. It is possible to notice that the dispersion with temperature shows a trend of opposite sign with respect to that in Fig. 7. Thus, an additional thermal perturbation must be taken into account.

In fact, during sensor normal operation the potentiometer is powered by the MIC5365-3.3YD5-TR LDO, that is turned off when no measures are done. This regulator is characterized by a non-ideal thermal stability: output voltage of this component was measured with a Keysight 34461a multimeter and compared against a temperature variation, from 25 °C to 70 °C (Fig. 9). A systematic effect was observed: voltage decreases while temperature rises. This trend, which over-compensates the thermal effects induced on the ADC, motivates the inverse proportionality between the acquired data and temperature which can be observed in Fig.8. It is worth noticing that the voltage regulator in the NUCLEO board used to generate the reference voltage for the ADC, has instead a way better behaviour, depicted in Fig. 9.

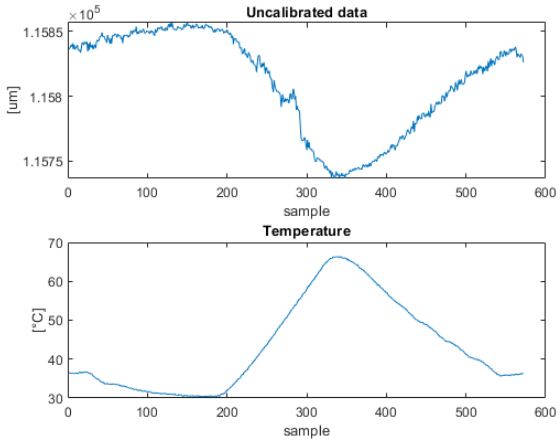

Fig. 8. Test with all the system under heating and cooling cycle. Above: averaged readings (Eq. (2)). Below: corresponding temperature cycle.

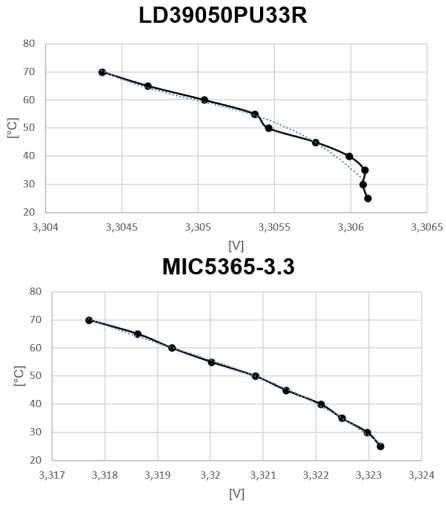

Fig. 9. LDOs output voltage vs. temperature.

Hence, a possible alternative consists in direclty supplying the potentiometer by an output pin of the MCU, thus exploiting the NUCLEO LDO only (the ADC shares the same power line used with the logic I/O of the micro-controller). The pin could be enabled only when a read is needed. However, similar

results to the ones in Fig. 8 were obtained. In this case, the issue was caused by the Rds_{on} factor of the devices composing the output CMOS buffer at the pin, characterized by a positive temperature coefficient. Rds_{on} value has been extracted for two different temperature values and compared to the expected difference computed using values in literature. At $27\,^{\circ}\mathrm{C}$ Rds_{on} = $26.8\,\Omega$, while at $57.5\,^{\circ}\mathrm{C}$ Rds_{on} = $31\,\Omega$. The increase estimated was 15.7% which is, for the same temperature interval, in good agreement with theory [7] (25.8%).

C. Thermal calibration of the prototype

The trend in Fig. 8 can be analyzed by placing the temperature on x-axis and the acquired $\overline{d}_{\mathrm{R}}$ on the y-axis. The results can be seen, for 30 deg and 60 deg aperture angle, in Fig. 10, in which the linear regression line for the corresponding acquired data set is also added. All the points are located very close to the line, without showing a significant elliptical trajectory, which would be a typical behaviour, instead, for a system characterized by long-term memory effects. It is therefore reasonable to confirm a linear dependence on temperature of the estimator of Eq. (2).

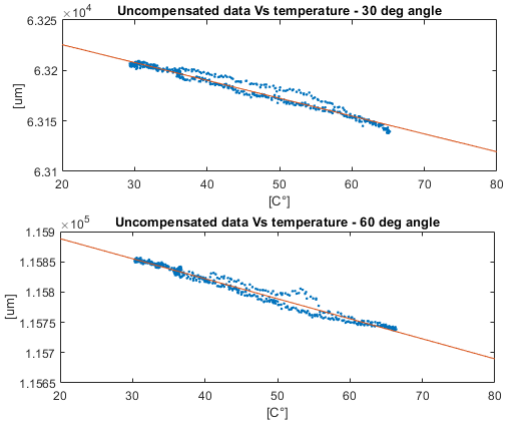

Fig. 10. Temperature cycles (Fig. 8, below) imposed to the overall prototype for two different plier apertures.

It is also experimentally observed that for the same temperature variation ΔT the variation of $\overline{d}_{\mathrm{R}}$ is proportional to the partition ratio. With this set of information it is possible to assume a relationship between temperature variations ΔT with respect to a reference $T^{(0)}$ and measured data $\overline{d}_R$ like the following:

$$\overline{d}_R = \overline{d}_R{}^{(0)}(1 + C_{\mathrm{th}} \times \Delta T) \tag{3}$$

where C_{th} is a constant thermal coefficient, which does not depend on the opening value of the plier, to be experimentally estimated and then used to compensate for temperature.

Two methods can be used for the estimation of the thermal coefficient. The first one would make use of the maximum variation ΔT and the corresponding variation of $\overline{d}_{\mathrm{R}}$, but in this way only two reference measurements would be considered. As more accurate option, C_{th} is obtained normalizing the angular coefficient of the best fit line computed with all the $\overline{d}_{\mathrm{R}}$ acquired while the plier is kept locked in a constant angle and after applying a cycle of temperature variations. Basically, this is the same as solving an overdetermined linear system of equations. This way to compute the coefficient is considered more proper because residual non-linearities with respect to temperature are considered and averaged out. In fact the result of R-Square test is quite accurate: at $60\,\mathrm{deg}$ opening angle, $C_{\mathrm{th}} = 0.31$ and $R^2 = 0,976$, while at $30\,\mathrm{deg}$ $C_{\mathrm{th}} = 0.29$ and $R^2 = 0,965$.

It's important to say that the ratio between ΔT and time must be not so high, because of the different thermal inertia of materials composing the system: if temperature slope is acceptably low, as in the case of a orchard, thermal dispersion can be accurately compensated. Results for the tests of Fig. 10, repeated after implementing the thermal calibration process based on Eq. (3) for $T_0 = 25.0\,^{\circ}\mathrm{C}$ and showing the calibrated output $\overline{d}_{R\text{-}T}$, are depicted in Fig. 12.

D. Plier thermal expansion

In order to take into account only the thermal dispersion effects suffered in the electronic hardware, all the datasets exploited so far were generated with fixed aperture angles (i.e., the plier was locked in the fulcrum with a bolt during temperature cycles). However, variations of environmental conditions cause variations also in the plier arm length. The coefficient of linear thermal expansion λ of ABS is known, so that the expansion ΔR with respect to $R^{(0)}$ at a reference temperature can be evaluated. We can rewrite Eq. (1):

$$d = d^{(0)} + 2 \cdot \Delta R \cdot \cos\left(\frac{\pi}{2} - \frac{\alpha(V_{out})}{2}\right) \tag{4}$$

By estimating ΔR for a measured ΔT with respect to T_0, Eq. (4) can be used to correct $\overline{d}_{R\text{-}T}$ also for plier thermal expansion/compression and obtain an output $\widehat{d}$ of the sensor fully compensated in temperature.

E. Calibration for non-linearities

The estimate $\widehat{d}$ still lacks for the compensation of all non-linear effects in the behaviour of the system (e.g., ADC non-linearity, geometrical dispersion in the fabrication process of the plier, etc.). Since all thermal effects were already taken into account, a single calibration curve extracted at $25.0\,^{\circ}\mathrm{C}$ throughout the full-scale by means of a reference caliber was sufficient to the purpose. The curve was interpolated through a cubic spline, whose coefficients were stored into the memory of the MCU to obtain in real-time, at each interrogation on the fruit diameter, the final linear output $\widehat{d}_L$. Fig. 11 summarizes all the calibration steps described.

IV. Results

In order to assess the performance of the overall calibration procedure, the following test is discussed. A pure-aluminum rod was inserted into the plier and, with the aid of a climatic chamber, a change in temperature was forced throughout the interval ($25\,^{\circ}\mathrm{C}$ - $70\,^{\circ}\mathrm{C}$) (Fig. 13, below). The variation in length caused by thermal expansion can be easily predicted knowing the coefficient of expansion $\lambda_{\mathrm{aluminum}}$ and by monitoring $\Delta T(t)$. The total temperature variation causes, for a

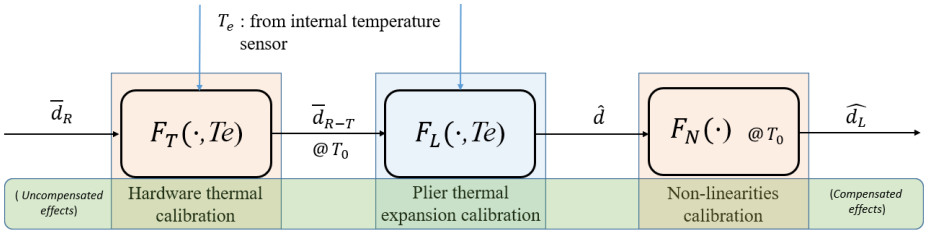

Fig. 11. The calibration procedure described by its stages.

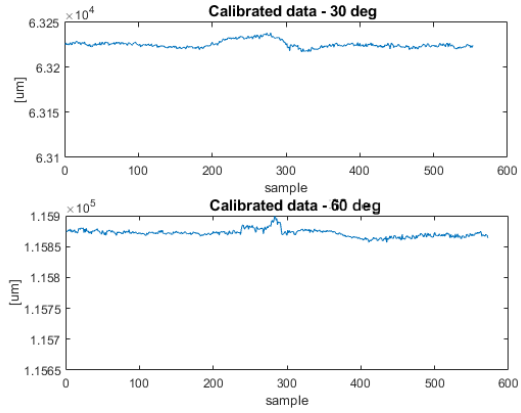

Fig. 12. Temperature cycles (Fig. 8, below) imposed to the overall prototype for two different plier apertures. Output of the sensor after thermal calibration.

starting length of $10.420\,\mathrm{cm}$ of the rod, an expected increment of $113\,\mu\mathrm{m}$. A peak-to-peak variation of $140\,\mu\mathrm{m}$ was measured

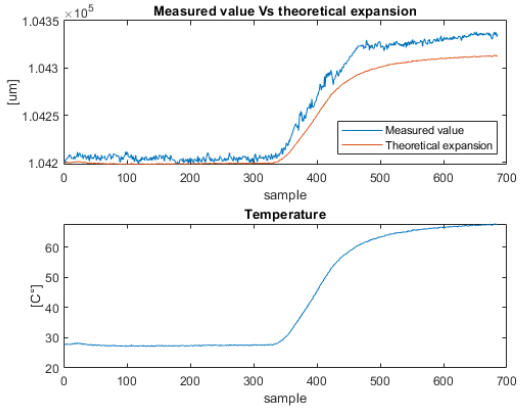

Fig. 13. Measurement of the length of a pure-aluminum rod during a temperature variation (below). Above: calibrated prototype vs. thermal model.

by the calibrated prototype. The difference with respect to the thermal model of the rod, i.e., $27\,\mu\mathrm{m}$, is approximately equal to the nominal quantization step of the sensor.

Fig. 14 shows the static response of the calibrated prototype compared to a reference obtained by means of a precision caliber. A total of 14 points were collected at $20\,^{\circ}\mathrm{C}$ throughout the actual range (2 cm - 12 cm) of the instrument in the final application (e.g., apples, oranges). By computing the rms deviation on the curve, the estimated standard uncertainty

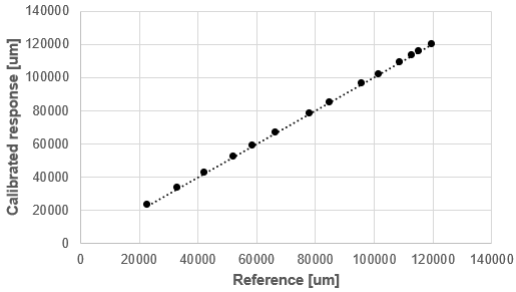

Fig. 14. Calibrated response of the prototype throughout its application range (2 cm - 12 cm).

corresponds to $70\,\mu\mathrm{m}$. This value can be converted into an effective quantization step $d_\mathrm{q} \cong 240\,\mu\mathrm{m}$ of the sensor, i.e., ENOB = 9.0 for a full-scale of 12 cm.

V. Conclusion

A prototype of a new sensor node for monitoring fruit growth was realized. Despite the use of low-cost components, quite high effective resolution was reached through the adoption of a multi-step calibration procedure, which allows to reduce uncertainty caused by all main internal and external perturbing factors. The architecture is thus robust to environmental conditions, and thanks to its full-scale and low power consumption the sensor can be deployed at the beginning of the ripening season with no need for further manning up to the harvest.

References

[1] A. Boini, L. Manfrini, G. Bortolotti, L. Corelli-Grappadelli, and B. Morandi, "Monitoring fruit daily growth indicates the onset of mild drought stress in apple," *Scientia Horticulturae*, vol. 256, p. 108520, 2019.

[2] J. Tromp, "Diurnal fruit shrinkage in apple as affected by leaf water potential and vapour pressure deficit of the air," *Scientia horticulturae*, vol. 22, no. 1-2, pp. 81–87, 1984.

[3] B. Klepper, V. D. Browning, and H. M. Taylor, "Stem diameter in relation to plant water status," *Plant Physiology*, vol. 48, no. 6, pp. 683–685, 1971.

[4] S. Link, M. Thiede, and M. v. Bavel, "An improved strain-gauge device for continuous field measurement of stem and fruit diameter," *Journal of Experimental Botany*, vol. 49, no. 326, pp. 1583–1587, 1998.

[5] B. Morandi, L. Manfrini, M. Zibordi, M. Noferini, G. Fiori, and L. C. Grappadelli, "A low-cost device for accurate and continuous measurements of fruit diameter," *HortScience*, vol. 42, no. 6, pp. 1380–1382, 2007.

[6] M. Thalheimer, "A new optoelectronic sensor for monitoring fruit or stem radial growth," *Computers and Electronics in Agriculture*, vol. 123, pp. 149–153, 2016.

[7] *AN-9010 MOSFET Basics*. [Online]. Available: https://www.onsemi.cn/pub/Collateral/AN-9010.pdf